# InAsSb-based detectors on GaSb for near-room - temperature operation in the mid-wave infrared

*A. P. Craig,[1,2] V. Letka,[1] M. Carmichael,[1,2] T. Golding,[2,3] and A. R. Marshall[1]
[1]Physics Department, Lancaster University, Lancaster, LA1 4YB, U.K.
[2]Amethyst Research Ltd., Kelvin Campus, West of Scotland Science Park, Glasgow, G20 0SP, UK.
[3]Amethyst Research Inc., 123 Case Circle, Ardmore, Oklahoma, 73401, USA.

*Corresponding author: a.craig1@lancaster.ac.uk

***Abstract:*** *III-Sb barrier detectors suitable for the mid-wave infrared were grown on GaSb by molecular beam epitaxy. Using both bulk-InAsSb and an InAsSb-InAs strained layer superlattice, operation close to room temperature was demonstrated with cut-off wavelengths of 4.82 µm and 5.79 µm, respectively, with zero-bias operation possible for the bulk-InAsSb detector. X-ray diffraction, temperature dependent dark current and spectral quantum efficiency were measured, and an analysis based on calculated specific detectivity carried out. 1/f noise effects are considered. Results indicate these optimized devices may be suitable as alternatives to InSb, or even HgCdTe, for many applications, especially where available power is limited.*

III-Sb alloys and quantum structures are being developed as alternatives to HgCdTe or InSb for mid-wave infrared (MWIR) detectors.[1-4] InSb generally requires cooling to 77 K for acceptable levels of performance and, whilst HgCdTe-based sensors generally still offer the highest signal to noise ratios, they suffer from a lack of large-area native substrates, an acute bandgap-compositional dependence at longer wavelengths,[5] uniformity issues and excessive cost. III-Sb alloys benefit from native 4” GaSb and 3” InAs substrates, lower cost, and the possibility for a wide range of heterostructures with lattice matched materials and alloys, e.g. AlAsSb, InAs, InAsSb or InGaAsSb.[6] Cut-off wavelengths between 1.7 µm and (at least) 12 µm can be achieved using various alloys and strained layer superlattices (SLS).[7-9] However, high dark currents due to trap-related processes and surface recombination are frequently problematic; the community has focussed extensively on developing III-Sb barrier detector designs, which address surface and defect related dark currents using AlSb-based electron-blocking barriers.[10-12] These barrier or “*nBn”* detectors were first reported using InAs and AlAsSb in 2006.[13] Since then, the design has been widely copied and extended to include InAsSb, e.g.[10] InGaAsSb [6] InAs-GaSb SLS e.g. [14,15] and InAsSb-InAs or “Ga free” SLS e.g. [7-9]. In addition to the references given, many others exist in the literature. InAsSb-InAs SLSs offer increased minority carrier lifetimes over InAs-GaSb designs. They are also simpler to grow, since only the Sb shutter needs to be actuated, and can effectively cover the MWIR atmospheric transmission window between ~4.5 – 5.5 μm to allow for free space comms and LIDAR applications, amongst others.

In this work, we report bulk-InAsSb and InAsSb-InAs SLS structures suitable for near-to-room-temperature operation with cut off wavelengths of 4.82 μm and 5.79 μm, respectively. For many applications, cooling requirements are heavily reduced, or even removed. For the bulk-InAsSb structure, zero bias operation is also demonstrated, achieved using a design combining a *p-n* junction with a barrier diode. The presence of a built-in field allows low-power bias-free operation, while carriers generated at the *p-n* junction through Shockley Read Hall or surface related processes cannot contribute to dark current. In reverse operating bias, electron current cannot flow (due to the presence of the wide-gap barrier) and corresponding hole transport is prevented due to charge neutrality. In other words, dark currents generated in the *p-n* junction layers do not contribute to the detector noise. While *p-i-n* InSb structures also offer zero bias operation, they generally require cooling to 77 K. Our devices offer strong quantum efficiencies: at 250 K the bulk material detector has a quantum efficiency of 30% at 4.0 μm, whereas the SLS has 17% at 5.0 μm. Moreover, these values were obtained with a single pass and without an antireflection coating. Given suitable design modifications, the detector bandwidth is also expected to be in the GHz range. The devices could be ideal for applications where available power or cooling is restricted, such as continuous remote monitoring.

Growth was carried out by solid source III-V molecular beam epitaxy (MBE) with SUMO® cells for Al, Ga and In, and valved cracker cells for As and Sb. The epilayer structures are shown in Fig. 1(a) and (b). GaSb substrates were prepared by degassing under vacuum at 350 C for 6-8 hours, before oxide removal at 530 C under constant $Sb_2$ flux. The samples were then cooled to 505 C for GaSb buffer layer growth. To optimize conditions in the growth chamber, the buffer was grown to a thickness of 2-3 μm over ~3 hours. The growth temperature for InAsSb bulk material was 450 C whereas the SLS layers were grown at 430 C. V-III ratios

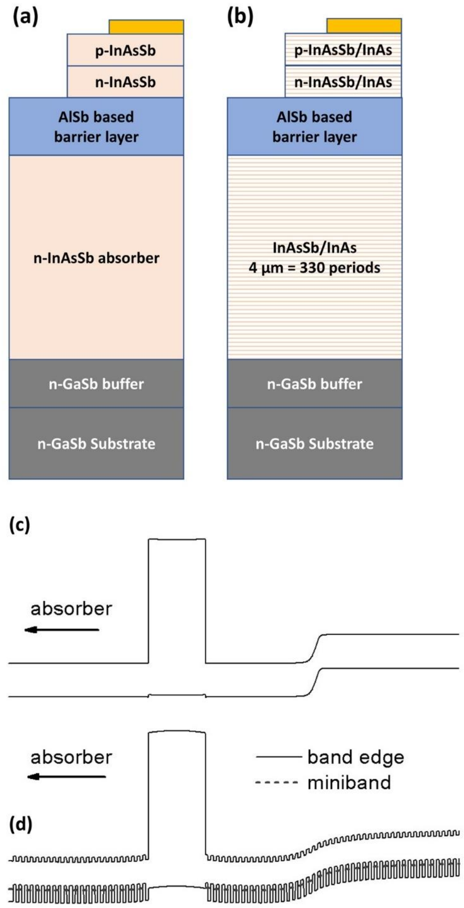


**Figure 1:** Layer structures for (a) bulk and (b) for the SLS. Band diagrams are given in (c) and (d), calculated by solving the Poisson Equation.

were maintained at ~1.6:1 and, in order to control the unintentional doping, a low level of Te dopant was used for the absorber layers.

Dark currents in infrared barrier detectors are known to vary nonlinearly with the absorber donor density $N_d$ (intentional or unintended). The diffusion current varies with $1/N_d$, but also with $1/\tau$, where $\tau$ the minority carrier lifetime. $\tau$ *falls* as $N_d$ increases.[16] Capacitance voltage measurements were therefore made to reveal $N_d$ in the *n*-type layers. As shown in Fig. 2(b), a background doping level of around $10^{16}$ cm$^{-3}$ was found for

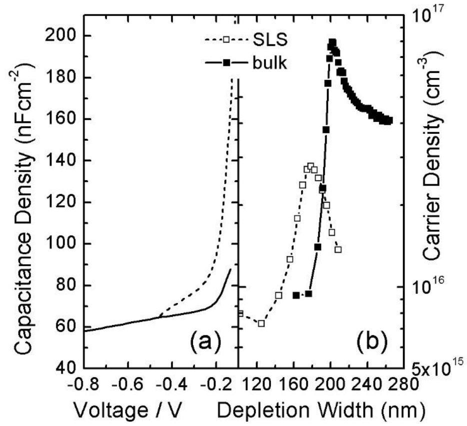


**Figure 2:** **(a)** Capacitance-voltage data for the bulk and SLS detectors. **(b)** The associated doping densities calculated by assuming single sided depletion in the *n*-type layers.

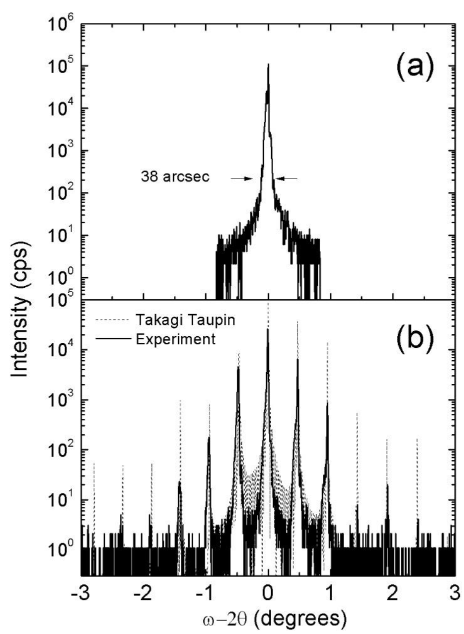


**Figure 3:** X-ray diffraction results and modelling **(a)** for the InAsSb bulk-material detector and **(b)** for the InAsSb-InAs SLS.

the *n*-InAsSb and *n*-type SLS layers above the barrier. The same doping concentration can be assumed for the absorber layers, which were grown under the same conditions. Free passage of holes, and hence strong quantum efficiency, was ensured by engineering the barrier layer composition using software based on the model solid approach and grown using AlSb-based materials at 505 C. The combination of the barrier diode with the *p-n* junction is illustrated in Figs. 1 (c) and (d).

In order to reduce dark currents due to crystalline defects in the material, and hence maximize 300 K detector performance, lattice matching was optimised using x-ray diffraction and the epilayer mismatch reduced to <500 ppm for the bulk-InAsSb and barrier layers. The x-ray results are given in Fig. 3 where the superlattice

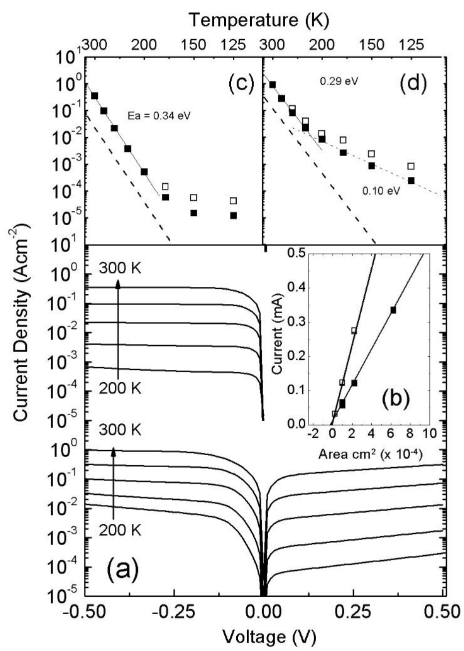


**Figure 4:** **(a)** Dark currents as a function of voltage and temperature for the bulk material detector (upper) and the SLS detector (lower). Part **(b)** shows the dark currents at 300 K as a function of area at -0.4 V for the bulk detector (solid symbols) and at -0.3 V for the SLS (open symbols). Parts **(c)** and **(d)** show Arrhenius plots for the bulk and SLS, respectively, where open symbols denote measurements without cold shielding. Activation energy fittings and dashed lines for Rule '07 are also shown.

fringes were fitted using software based on the Takagi-Taupin equations.[17] The Sb content was dilute to achieve a 0.225 eV effective bandgap at 250 K. Whilst trap related or Auger dark currents dominate at high temperature, low temperature detector performance is ultimately limited by the background photon flux due to the 300 K scene. This occurs below the BLIP (background limited infrared photodetection) temperature, and further cooling without cold shielding is ineffective due to the photon noise. Fig. 4(a) shows dark currents as a function of voltage and temperature, while part (b) shows the effective suppression of surface currents by the barrier layer: the current at operating bias is plotted as a function of device area, showing close to zero intercept. Parts (c) and (d) show Arrhenius plots at -0.3 V. Dark current activation energies can be used to reveal the dominant dark current process, and hence further reduce it. For the bulk detector this is close to the full 4 K bandgap of the absorber (0.345 eV). Similarly, for the SLS, the effective bandgap is calculated to be 0.30 eV (also at 4 K).[18] This indicates Auger limited dark currents. The comparison with the low temperature bandgap is intentional, in other words, the activation energy is not thought to vary as temperature increases.[19] A second gradient is observed for the SLS detector below roughly 200 K. We attribute this to a shift from the Auger limited regime to a weak tunnelling process. The shielded measurements diverge from the data below approximately 200 K for both detectors. Whilst conceding that HgCdTe offers lower leakage currents, as indicated by the Rule '07 heuristic lines on the figures, the difference is often less than one order of magnitude at operating temperature.

Detector performance is usually limited by the Shot or thermal noise on the dark current, which varies with its square root. The specific detectivity gives a figure of merit for the signal to noise ratio. The sum of the theoretical Shot and thermal noise currents is given by

$$I_n^2 = 2qI_0 + 4kT/R_d \qquad (1)$$

where q is the elementary charge, $I_0$ the DC dark current, k the Boltzmann constant, T the detector temperature and $R_d$ the dynamic resistance. However, a more accurate determination of the total system noise can be obtained using a Signal Analyzer or Spectrum Analyser together with a preamplifier. This will reveal noise due to interaction with the amplifier, or 1/f effects, and provide a real-world indication of performance.

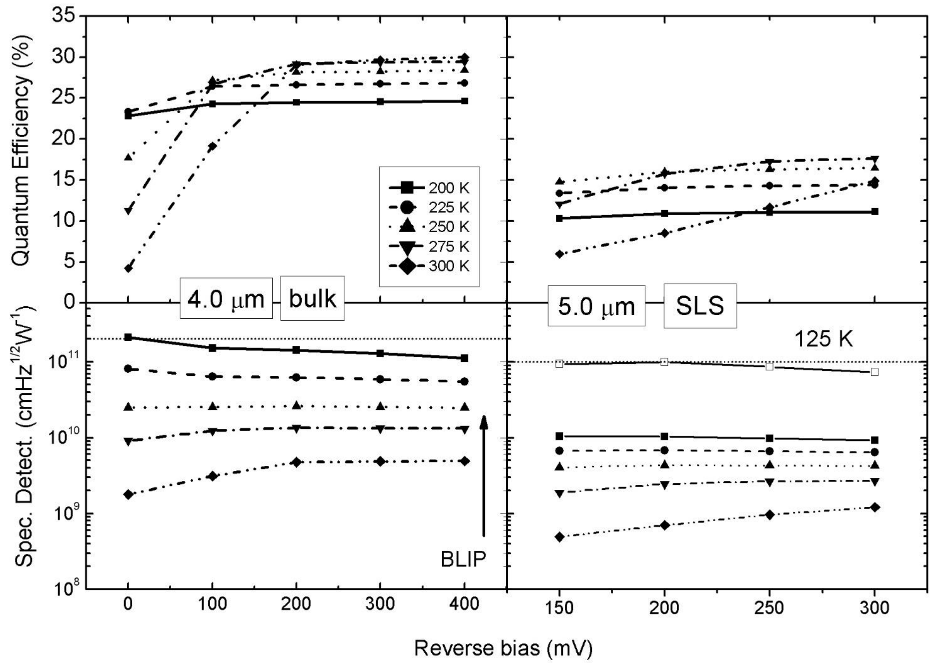


**Figure 5:** Quantum efficiency and specific detectivity at 4.0 μm for the bulk InAsSb detector and at 5.0 μm for the SLS, as determined using Eq. 2 and the data from Fig. 4. For the SLS, a further line is included for 4.5 um and 125 K. Dotted lines indicate the BLIP limits for f/2 optics [20].

Once $I_n^2$ is known, all that is left is to find the detector responsivity, $R_i$. While this can be achieved using a blackbody at an appropriate temperature, we prefer to obtain full spectral dependence using a calibrated FTIR spectrometer. D* then can be obtained from,

$$D^* = R_i / \sqrt{2qJ + 4kT/R_dA_d} \qquad (2)$$

or

$$D^* = R_i / \sqrt{I_n^2} \qquad (3)$$

where J is the dark current density and $R_dA_d$ the resistance area product (which is simply $dV/dJ$ by numerical approximation).

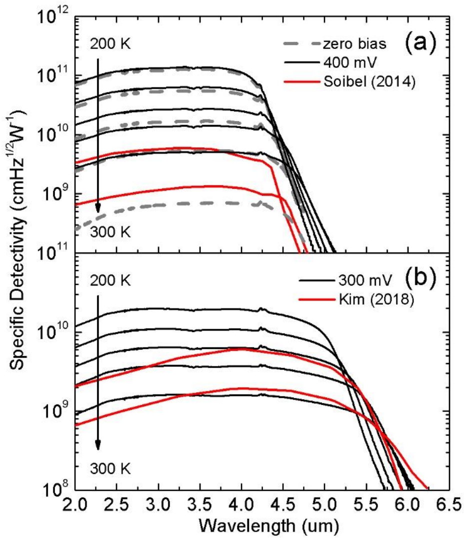


**Figure 6:** Spectral specific detectivity found using Eq. 2 for **(a)** the bulk detector, at 400 mV and zero bias, in steps of 25 K. Reference data from [21] is also given at 250 K and 300 K. **(b)** for the SLS, also in steps of 25 K, with reference data at 253 K and 295 K.[22]

Quantum efficiency and specific detectivity are shown in Fig. 5. The former increases monotonically with bias for both detectors, reflecting improved extraction of photogenerated carriers. For the bulk material detector, a zero bias response is also included: this falls significantly between 200 – 300 K due to an increase in the recombination processes. At finite bias, both detectors exhibit a weaker temperature dependence. The specific detectivity exhibits the opposite behaviour to the quantum efficiency, falling monotonically with temperature. In turn, this reflects the increase in the detector noise as the dark currents increase, which dominates over the increase in quantum efficiency. The shape of the specific detectivity is to some extent flat with applied bias but increases gradually with bias for the bulk-InAsSb detector between 275 – 300 K (owing to increased quantum efficiency) but falls with bias at lower temperatures (owing to increased dark currents). Strong performance at 300 K confers advantages in applications where limited cooling is available (perhaps due to limited power), e.g. continuous remote monitoring. Above 200 K, the SLS performance improves with bias. BLIP conditions are included for f/2 optics and 300 K scene temperature, taken from [20]. These coincide with the data at around 200 K for the bulk detector and 125 K for the SLS, and differ from the temperature at which the dark currents diverge from the shielded measurements in Fig 4(c) and (d) owing to the absence of f/2 optics and the low emissivity of the probe station interior. When the detector performance exceeds the BLIP limits, the lower level of performance applies in practice. Full spectral dependence for the D* is shown in Fig. 6. Low-power 2-stage thermoelectric (TE) coolers suitable for these detectors can readily achieve temperatures of 250 K or below and cut-off wavelengths at 250 K, 275 K and 300 K are shown in Table 1 (found by extrapolating the squared response vs 1/energy). The end user can then select between 300 K operation or low power TE cooling. By operating at zero bias, the device power can also be reduced and the zero bias detectivity of the bulk detector is close to the 300 mV response between 200 – 250 K. Uncooled operation is also possible for the SLS detector. Referring to Fig. 5, the D* at 300 K varies by less than a factor of 2 between 150 and 300 mV applied bias and the dark currents in Fig. 4(a) are <1 $Acm^{-2}$ for room temperature operation. Reference data given in (a) for Soibel (2014) [21] is exceeded by our devices at finite bias at all temperatures. At 275 K and zero bias, our detector exhibits performance comparable to [21] at 250 K. The applied bias in [21] is not listed explicitly but appears to be ~300 mV (based on Fig. 3 in the reference). Ref [22] also reports detectors using InAsSb-InAs SLS and the level of performance and cut-off wavelength are comparable to our own. However, devices in [22] benefit from an antireflective coating, obtaining 74% quantum efficiency at 4.24 μm. The dark current density is further reported to be similar; at 300 K and 250 K values of 1.17 $A/cm^2$ and 0.1 $A/cm^2$ compare with 0.9 $A/cm^2$ and 0.09 $A/cm^2$ for our devices.

The preceding analysis considers detector noise occurs only due to Shot and thermal noise contributions. This is a common assumption in the literature, and very little work has been carried out to measure the noise frequency spectrum in barrier detectors. To address this concern, we present an analysis of the measured noise

| | 250 K | 275 K | 300 K |
|---|---|---|---|
| **Bulk InAsSb** | 4.64 | 4.77 | 4.82 |
| **InAsSb-InAs SLS** | 5.50 | 5.67 | 5.79 |

**Table 1:** Cut off wavelengths in μm for both detectors at temperatures within the range of 2-stage TE coolers.

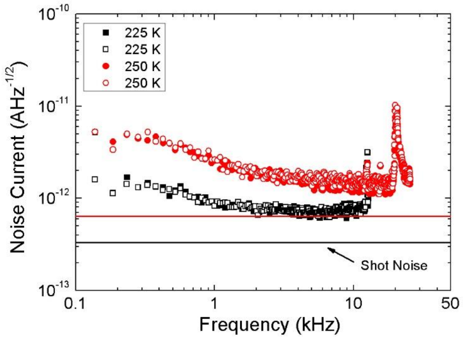


**Figure 7:** Noise current as function of frequency for the bulk-InAsSb detector. Results from two devices are shown; these were typical results from a larger sample.

in Fig. 7. The figure includes lines indicating the levels of Shot noise expected based on dark current measurements carried out for the specific devices analysed immediately beforehand. The level of thermal (Johnson) noise was less than the Shot noise to the extent that is has been excluded for our analysis. In the limit f→∞ the measured noise exceeds the calculated Shot noise by approximately a factor of 2, an effect we attribute to noise from the amplifier. Moreover, the noise current rises with 1/f dependence: at 300 Hz the measured noise is higher by a factor of ~4 at 225 K and ~7 at 250 K. The 1/f component of the noise intersects the frequency independent component at 1.8 kHz at 225 K and 2.8 kHz at 250 K. In other words, barrier detector devices, which are in some sense a hybrid between photovoltaic detector and photoconductor, share some of the 1/f noise properties of photoconductors.

This work has demonstrated barrier detectors on GaSb based on III-Sb materials suitable for mid-wave infrared detection at or close to 300 K. At 300 K, cut-off wavelengths of 4.82 μm and 5.79 μm were measured for devices with bulk-InAsSb and InAsSb-InAs SLS absorbers, respectively. At the same temperature, specific detectivity exceeded $5 \times 10^9$ and $1 \times 10^9$ $\mathrm{cmHz^{1/2}W^{-1}}$ at 4.0 μm and 5.0 μm, respectively. Zero bias operation was demonstrated for the 4.82 μm detector; conferring advantages for applications where available power is limited. A noise spectral measurement was carried out revealing the presence of finite 1/f noise. These optimized devices are suitable for low power applications through near-room temperature operability and are intended to replace HgCdTe or InSb for many applications. This work was supported through the dstl Space

Programme via the DASA Space-to-Innovate Phase I competition to develop a III-V barrier-diode MWIR detector for space applications under grant number DSTLX1000140474. The data that support the findings of this study are available from the corresponding author upon reasonable request.

# References

[1] P. Martyniuk and A. Rogalski, Opt Quant Electron (2014) 46 581–591

[2] D.Z. Ting, A. Soibel, A. Khoshakhlagh, S.A. Keo, S.B. Rafol, L. Hoglund, E.M. Luong, A.M. Fisher, C.J. Hill, and S.D. Gunapala, Journal of Elec Materi 48, 6145–6151 (2019).

[3] "Antimonide-based Infrared Detectors: A New Perspective" A. Rogalski, M. Kopytko and P. Martyniuk, (SPIE Press 2018).

[4] A. Rogalski, "InAsSb INFRARED DETECTORS" Prog Quant Electr 1989, Vol 13, pp 191-231 (1989).

[5] A. Rogalski. "HgCdTe infrared detector material: History, status and outlook." Reports on Progress in Physics. 68 2267 (2005).

[6] A. P. Craig, M. Jain, G. Wicks, T. Golding, K. Hossain, K. McEwan, C. Howle, B. Percy and A. R. J. Marshall, Appl. Phys. Lett. 106, 201103 (2015);

[7] A. Haddadi, G. Chen, R. Chevallier, A.M. Hoang and M. Razeghi, Appl. Phys. Lett. 105, 121104 (2014).

[8] D. Wu, Q. Durlin, A. Dehzangi, Y. Zhang, and M. Razeghi, Appl. Phys. Lett. 114, 011104 (2019).

[9] A.M. Hoang, G. Chen, R. Chevallier, A. Haddadi, and M. Razeghi, Appl. Phys. Lett. 104, 251105 (2014);

[10] A. P. Craig, M. D. Thompson, Z.-B. Tian, S. Krishna, A. Krier and A. R. J. Marshall Semicond. Sci. Technol. 30 (2015) 105011

[11] E. Plis, H.S. Kim, G. Bishop, S. Krishna, K. Banerjee, and S. Ghosh, Appl. Phys. Lett. 93, 123507 (2008);

[12] G.R. Savich, J.R. Pedrazzani, S. Maimon, and G.W. Wicks, Phys. Status Solidi C, 10, 2540–2543 (2010).

[13] S. Maimon and G. W. Wicks (2006) Appl. Phys. Lett. 89 151109.

[14] G. Bishop, E. Plis, J. B. Rodriguez, Y. D. Sharma, L. R. Dawson and S. Krishna, J. Vac. Sci. Technol. B 26(3), 1145 (2008).

[15] J. B. Rodriguez, E. Plis, G. Bishop, Y. D. Sharma, H. Kim, L. R. Dawson and S. Krishna, Appl. Phys. Lett. 91, 043514 (2007).

[16] E. A. Kadlec, B. V. Olson, M. D. Goldflam, J. K. Kim, J. F. Klem, S. D. Hawkins, W. T. Coon, M. A. Cavaliere, A. Tauke-Pedretti, T. R. Fortune, C. T. Harris, and E. A. Shaner, Appl Phys. Lett. 109 261105 (2016).

[17] W.J. Bartels, J. Hornstra and D.J.W. Lobeek, Acta Cryst. A42, 539-545. (1986).

[18] M. P. C. M. Krijn, Semicond. Sci. Technol. 6, 27 (1991).

[19] P. Klipstein, in Proc. SPIE 6940, Infrared Technology and Applications XXXIV, 69402U (2008).

[20] N. Sclar, Progress in Quantum Electron. 9, 149, 1984.

[21] A. Soibel, C. J. Hill, S. A. Keo, L. Hoglund, R. Rosenberg, R. Kowalczyk, A. Khoshakhlagh, A. Fisher, D. Z.-Y. Ting, and S. D. Gunapala, Appl. Phys. Lett. 105 023512 (2014).

[22] J. Kim, H. Yuan, J, Kimchi, J. Lei, E. Rangel, P. Dreiske, A. Ikhlassi, Proc. Spie. 10624, Infrared Technology and Applications XLIV, 1062412 (2018).

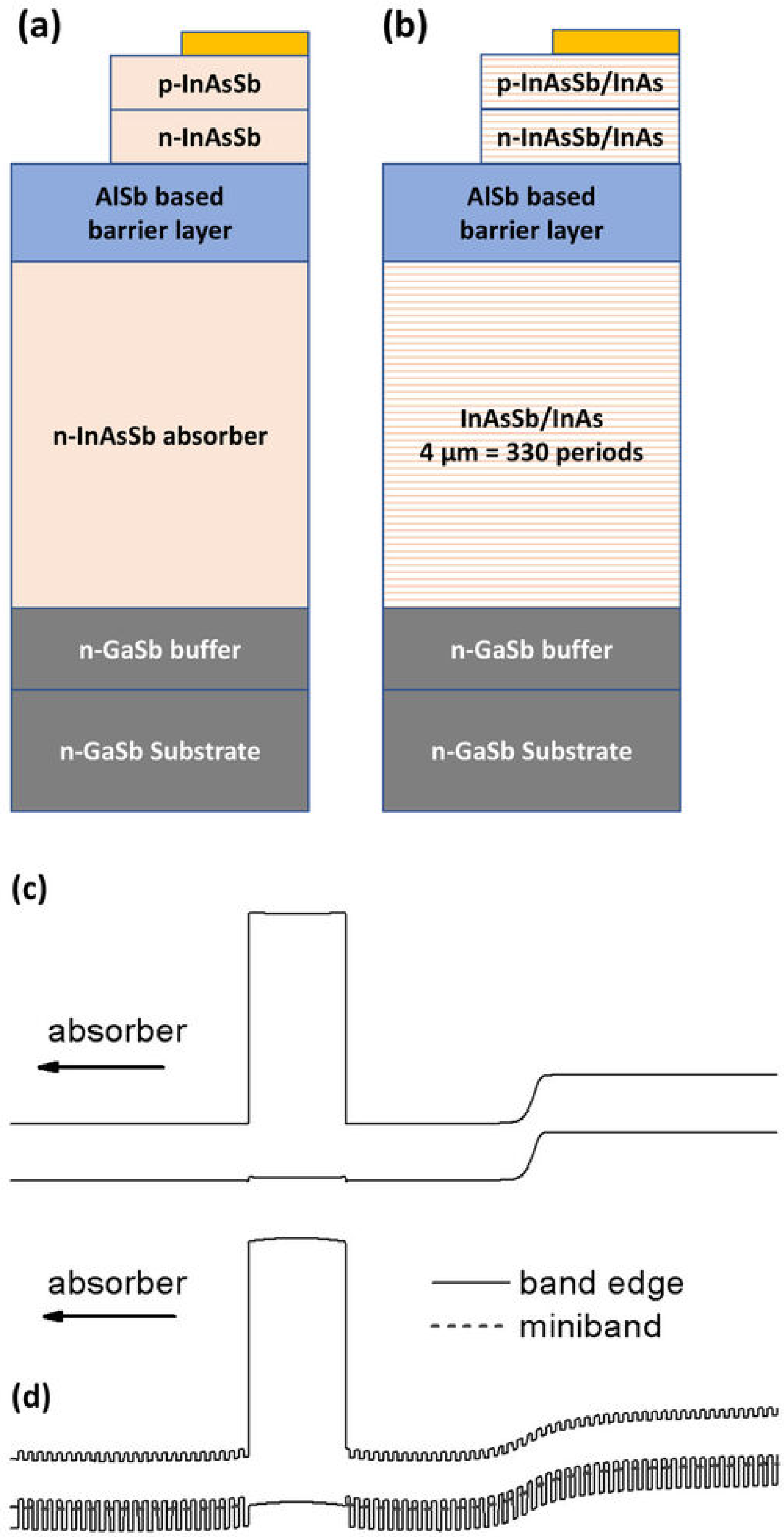
(a)
p-InAsSb
n-InAsSb
AlSb based barrier layer
n-InAsSb absorber
n-GaSb buffer
n-GaSb Substrate
(b)
p-InAsSb/InAs
n-InAsSb/InAs
AlSb based barrier layer
InAsSb/InAs
4 µm = 330 periods
n-GaSb buffer
n-GaSb Substrate
(c)
absorber
absorber
band edge
miniband
(d)

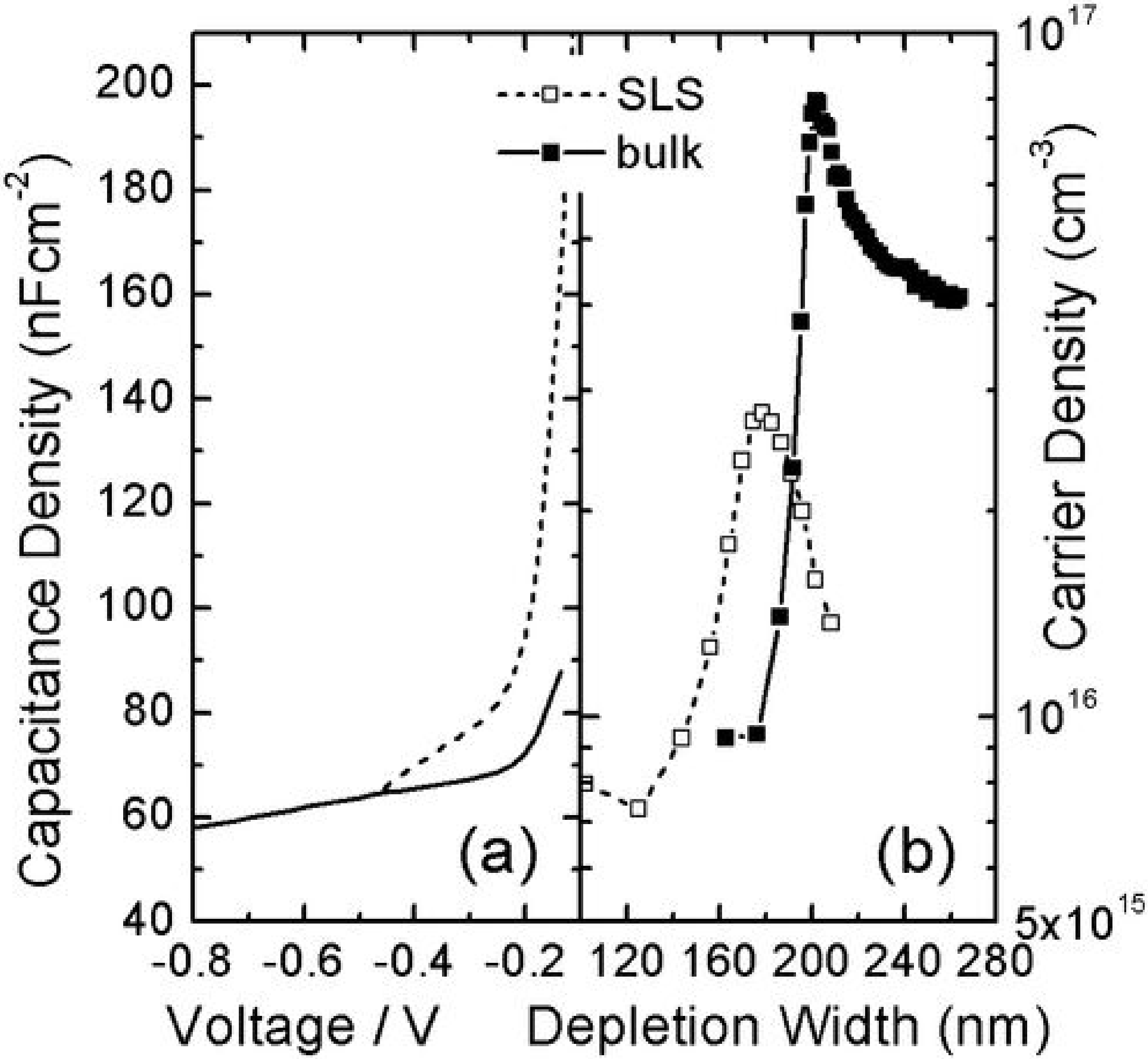
SLS
bulk
Capacitance Density (nFcm$^{-2}$)
Carrier Density (cm$^{-3}$)
(a)
(b)
200
180
160
140
120
100
80
60
40
$10^{17}$
$10^{16}$
$5x10^{15}$
-0.8
-0.6
-0.4
-0.2
120
160
200
240
280
Voltage / V
Depletion Width (nm)

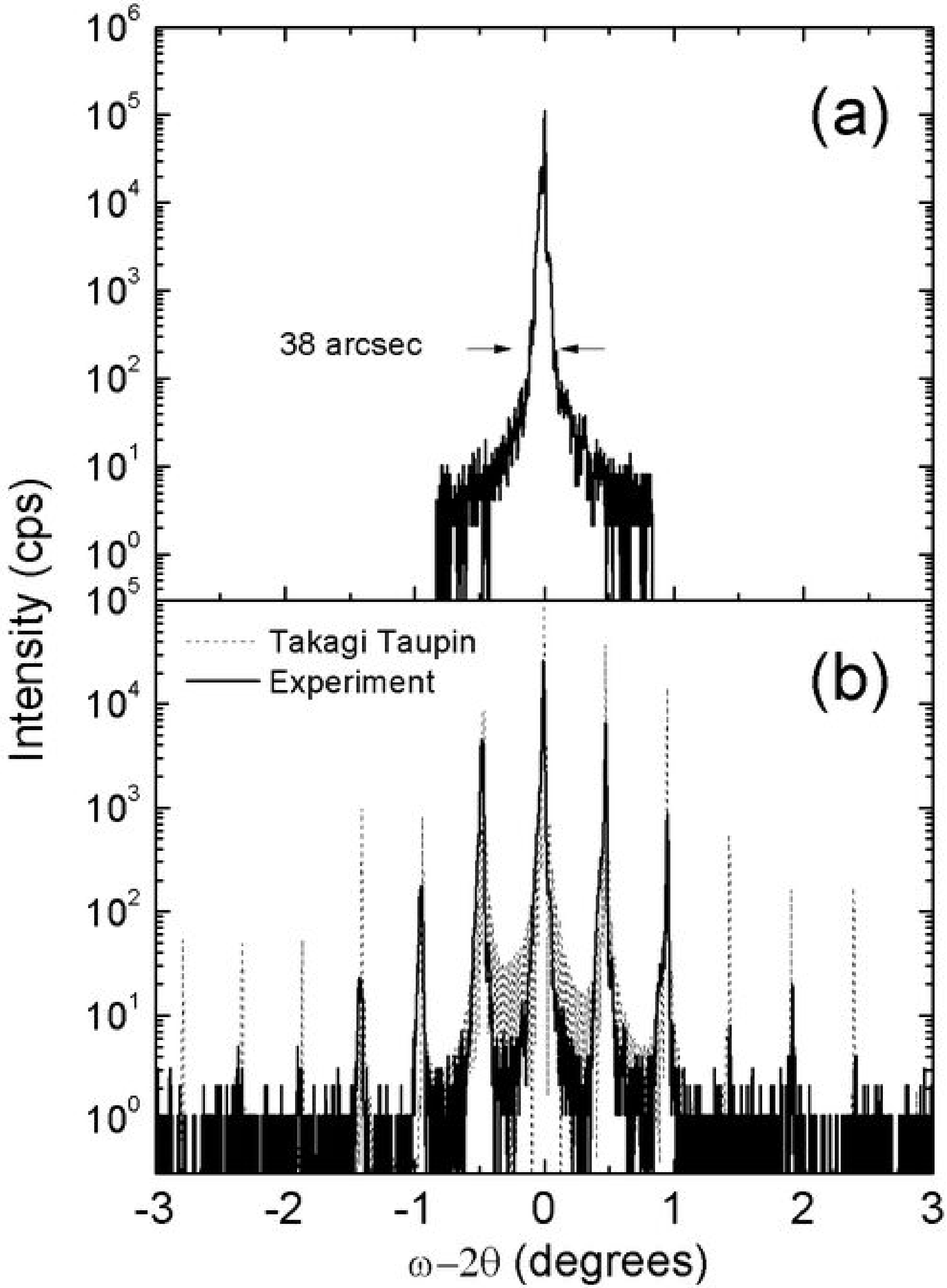
(a)
38 arcsec
(b)
Takagi Taupin
Experiment
Intensity (cps)
$\omega-2\theta$ (degrees)

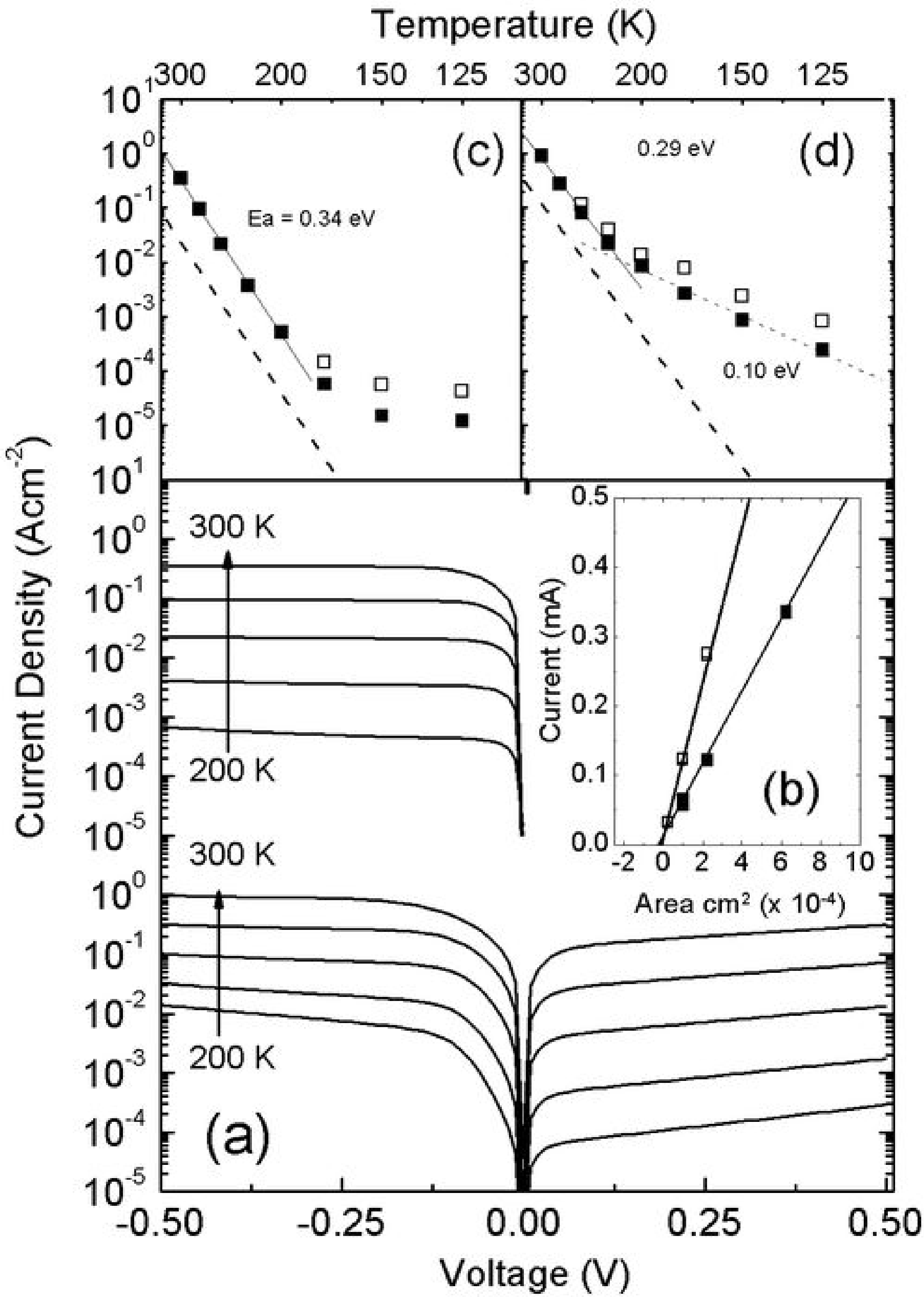

Temperature (K)
300
200
150
125
(c)
Ea = 0.34 eV
(d)
0.29 eV
0.10 eV
Current Density (Acm$^{-2}$)
300 K
200 K
300 K
200 K
(a)
(b)
Current (mA)
Area cm$^2$ (x 10$^{-4}$)
Voltage (V)

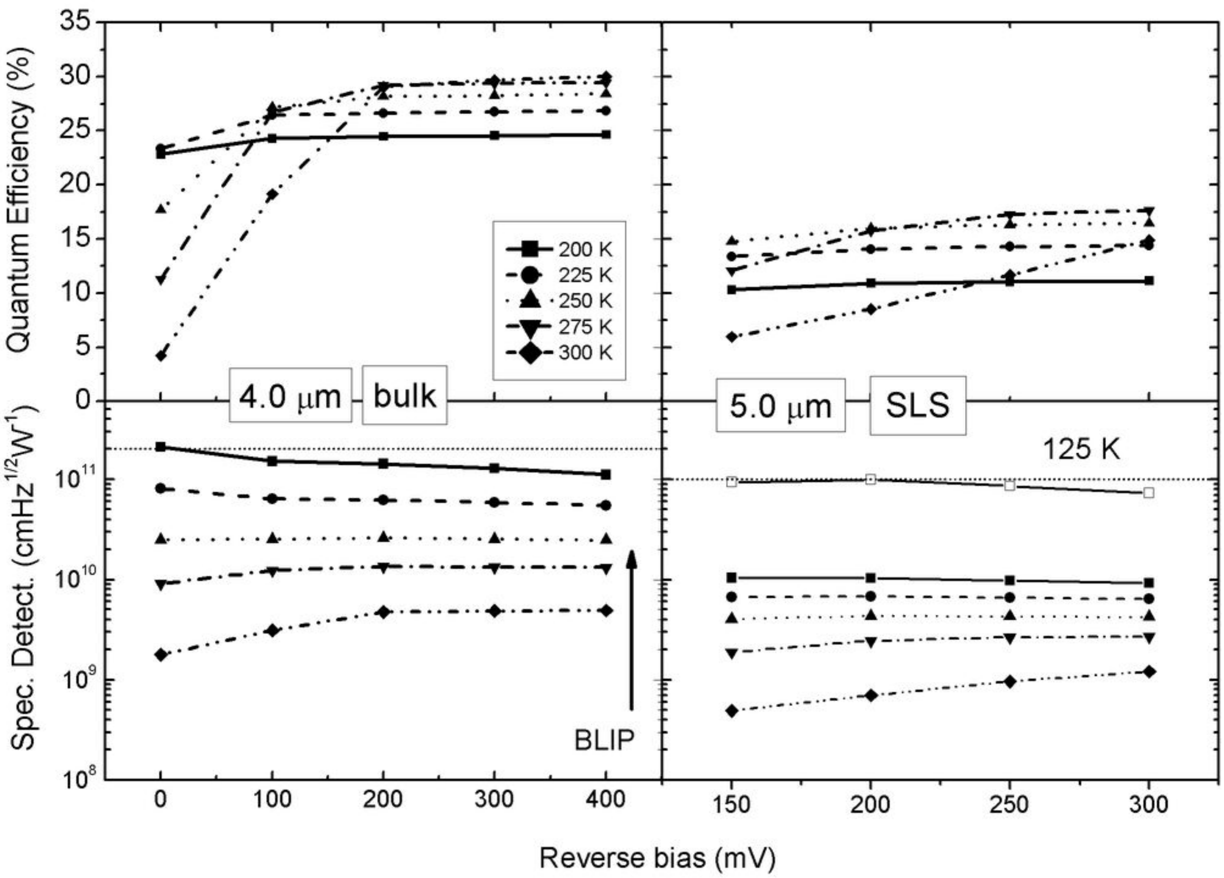
Quantum Efficiency (%)
Spec. Detect. (cmHz$^{1/2}$W$^{-1}$)
200 K
225 K
250 K
275 K
300 K
4.0 μm
bulk
5.0 μm
SLS
125 K
BLIP
Reverse bias (mV)

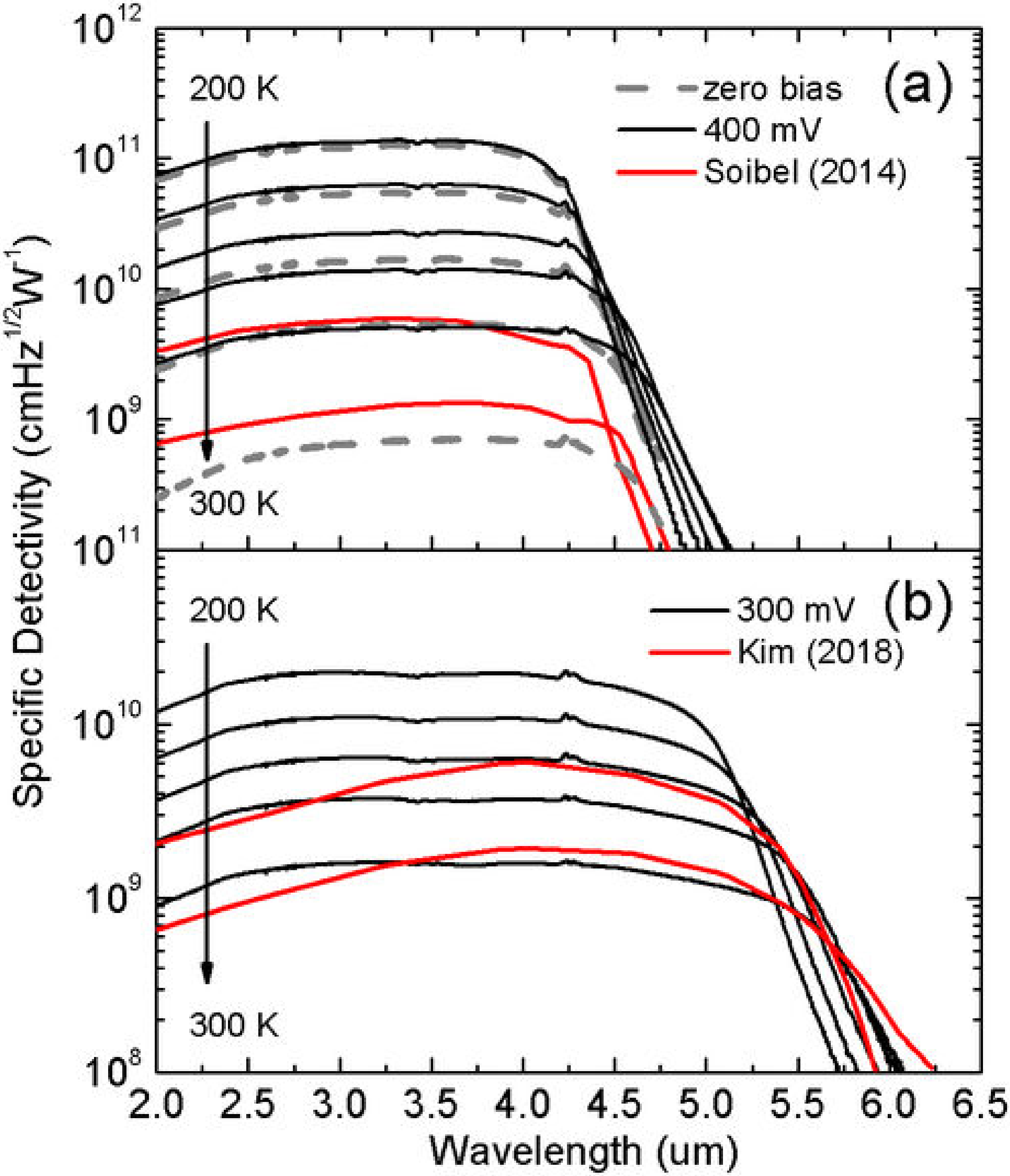
(a)
200 K
300 K
zero bias
400 mV
Soibel (2014)
(b)
200 K
300 K
300 mV
Kim (2018)
Specific Detectivity (cmHz$^{1/2}$W$^{-1}$)
Wavelength (um)
$10^{12}$
$10^{11}$
$10^{10}$
$10^{9}$
$10^{11}$
$10^{10}$
$10^{9}$
$10^{8}$
2.0
2.5
3.0
3.5
4.0
4.5
5.0
5.5
6.0
6.5

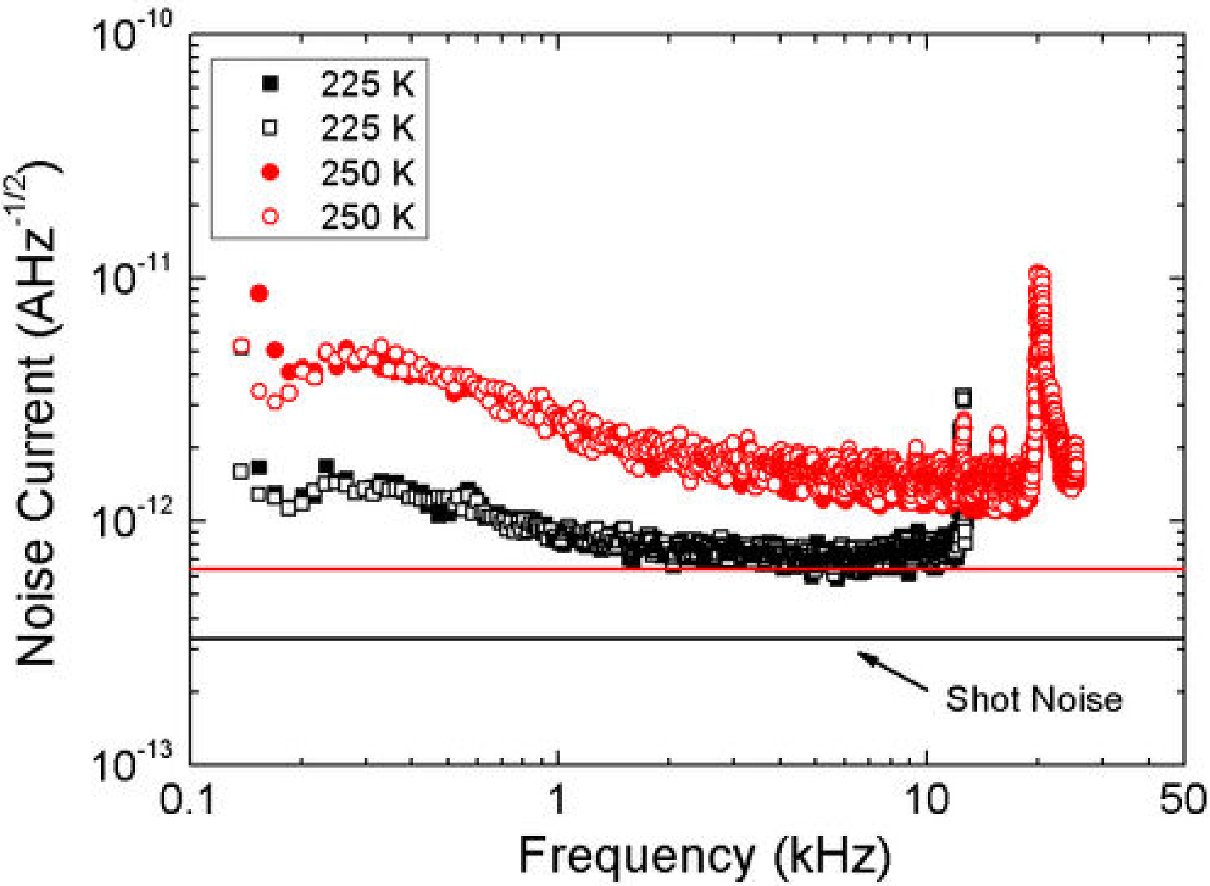
225 K
225 K
250 K
250 K
Shot Noise
Noise Current (AHz$^{-1/2}$)
Frequency (kHz)
$10^{-10}$
$10^{-11}$
$10^{-12}$
$10^{-13}$
0.1
1
10
50